AGU PUBLICATIONS

JGR

Journal of Geophysical Research: Solid Earth

RESEARCH ARTICLE

10.1002/2016JB013314

Key Points:
- Kinematic scenario ruptures can be created with the K-L expansion
- Scenario ruptures are used to create synthetic GNSS data
- Synthetic data are important for hazards and warning

Supporting Information:
- Supporting Information S1

Correspondence to:
D. Melgar,
dmelgar@berkeley.edu

Citation:
Melgar, D., R. J. LeVeque, D. S. Dreger, and R. M. Allen (2016), Kinematic rupture scenarios and synthetic displacement data: An example application to the Cascadia subduction zone, *J. Geophys. Res. Solid Earth*, *121*, 6658–6674, doi:10.1002/2016JB013314.

Received 27 JUN 2016
Accepted 28 AUG 2016
Accepted article online 31 AUG 2016
Published online 21 SEP 2016

Kinematic rupture scenarios and synthetic displacement data: An example application to the Cascadia subduction zone

Diego Melgar[1], Randall J. LeVeque[2], Douglas S. Dreger[1], and Richard M. Allen[1]

[1]Seismological Laboratory, University of California, Berkeley, California, USA, [2]Department of Applied Math, University of Washington, Seattle, Washington, USA

Abstract Scenario ruptures and ground motion simulation are important tools for studies of expected earthquake and tsunami hazards during future events. This is particularly important for large (M_w8+) and very large (M_w8.5+) events for which observations are still limited. In particular, synthetic waveforms are important to test the response of earthquake and tsunami warning systems to large events. These systems are not often exercised in this manner. We will show an application of the Karhunen-Loève (K-L) expansion to generate stochastic slip distributions of large events with an example application to the Cascadia subduction zone. We will discuss how to extend the static slip distributions obtained from the K-L expansion to produce kinematic rupture models and generate synthetic long-period displacement data at the sampling rates of traditional Global Navigation Satellite Systems (GNSS) stations. We will validate the waveforms produced by this method by comparison to a displacement-based ground motion prediction equation obtained from GNSS measurements of large earthquakes worldwide.

1. Motivation

Due to the increase in geophysical monitoring infrastructure, large events of the 21st century have been measured extensively; in spite of this we still have only a limited view of very large earthquakes. Observations are circumscribed to only a few geographic regions, and because of their long recurrence intervals, the variability of the sources that have been observed is small. For example, prior to the 2004 M_w9.2 Sumatra and M_w9.0 Tohoku-oki earthquakes, ground motions from very long sources (500+ km) and events with very large amounts of slip (30+ m) had not been observed with modern sensing technologies. This is a challenge for hazard assessments, particularly for regions with known large ruptures in the historical and geologic records but with few or no events in instrumental times. In this work we will present a method for generating scenario ruptures and displacement ground motion data. To exemplify the method we will use the Cascadia subduction zone as the tectonic setting. Cascadia is notoriously quiescent in terms of seismicity; it has not had a significant event since the 2001 M_w6.8 Nisqually intraslab earthquake [*Ichinose et al.*, 2004] and the 1992 M_w7.1 Cape Mendocino earthquake before it [*Li et al.*, 1993]. Cascadia has not experienced a large (M8+) rupture since the 1700 *M*9.0 earthquake [*Satake et al.*, 2003].

Parallel to the growth in the understanding of the hazards that large megathrust ruptures pose to societies, there has been a proliferation of earthquake early warning (EEW) technologies designed to mitigate the impact of such events. Algorithms based on traditional seismic data (ground acceleration and velocity) are in several stages of deployment in many tectonically active regions [i.e., *Allen et al.*, 2009]. For these seismic-only approaches magnitude saturation, the condition by which magnitudes are systematically underestimated for large events, is an inherent limitation [e.g., *Hoshiba and Ozaki*, 2014]. To ameliorate this, high-rate (1–10 Hz) measurements of ground motion displacements from Global Navigation Satellite Systems (GNSS) are becoming a mainstay of EEW [*Bock and Melgar*, 2016] with many different algorithms under development. GNSS data can accurately measure long-period strong motion displacements down to the static offset (0 Hz), and thus, algorithms that harness these measurements do not suffer from saturation. One limitation of GNSS-based EEW techniques is that they require longer wait times for accurate magnitude determination.

EEW systems that rely on seismic data are routinely stress-tested by smaller magnitude events that are well recorded by broadband and strong motion sensors. Problems, shortcomings, unexpected results, and the general performance of algorithms can then be assessed as a matter of routine. EEW algorithms that rely on GNSS cannot be tested in this way. The elevated noise levels in GNSS data typically preclude measuring events smaller than M_w6–6.5 at close in distances (tens of kilometer) and M_w7 at longer distances (hundreds of kilometer). There is a need for realistic scenarios and waveforms that can be used to assess the performance of EEW algorithms that rely on GNSS data as input.

In addition to EEW there is pressing need for local tsunami early warning (TEW) systems that can rapidly assess large sources and, if possible, forecast tsunami amplitudes for the regions immediately adjacent (local warning) to these earthquakes, where the time scales of warning are on the order of only a few minutes to an hour [*Melgar et al.*, 2016a]. Local TEW systems are evolving toward a hybrid approach that relies on both seismic and geodetic measurements. Much like in the EEW case, local TEW can benefit from a coherent framework for rupture scenario generation.

Previous scenario simulations [e.g., *Olsen et al.*, 2008] showed the importance of simulation in an area as seismically quiescent as Cascadia. Here we will demonstrate an application of the Karhunen-Loève (K-L) expansion method for generating random, but realistic, static slip patterns [*LeVeque et al.*, 2016]. With the Cascadia subduction zone as a focus area we will show how to extend the K-L expansion method to kinematic rupture scenarios and use it to generate synthetic GNSS data at regional stations. In this work we produce and make available (see the Acknowledgements section) 1300 rupture scenarios and their associated synthetic waveforms for events spanning magnitudes between M_w7.8 and M_w9.3 (see the Acknowledgments section and Figures S1–S4 in the supporting information). The code used to generate them is also made freely available (see the Acknowledgements section).

Frameworks exist for validating synthesized ground motions [e.g., *Dreger et al.*, 2015; *Goulet et al.*, 2015]; these rely on comparison of synthesized data to acceleration and velocity parameters such as peak ground acceleration (PGA), peak ground velocity (PGV), or spectral accelerations (Sa) from ground motion prediction equations (GMPEs). We argue that to validate synthetic GNSS data displacement-based ground motion parameters should be used. Modern GMPEs are not well suited to characterize displacement metrics, especially for strong ground motions where the static offset (fling in earthquake engineering parlance) and, in general, long-period motions are substantial [*Kamai and Abrahmson*, 2015]. This is a consequence of the standard processing applied to strong ground motion records necessary to minimize baseline offsets [*Boore and Bommer*, 2005] that effectively biases displacement metrics for large events [*Melgar et al.*, 2013, 2015]. Instead, for validating synthetic GNSS data, we will rely on a peak ground displacement (PGD) scaling law and GMPE developed directly from GNSS data worldwide for events in the M_w6–9 range [*Crowell et al.*, 2013; *Melgar et al.*, 2015].

2. Methods and Assumptions

2.1. Fault Geometry and Station Distribution

The exact 3-D geometry of the Cascadia subduction zone has been a topic of debate. The Slab 1.0 worldwide model of subduction zones relies on historic earthquake catalogues and centroid moment tensor solutions for definition of the megathrust geometries worldwide [*Hayes et al.*, 2012]. For the quiescent Cascadia subduction zone, the Slab 1.0 model relies on the correlation of the sparse seismicity with a number of active and passive crustal structure surveys [*McCrory et al.*, 2012]. We rely on this 3-D geometry for our fault definition (Figure 1) and discretize it into 963 triangular elements (subfaults) by using a finite element mesher. The downdip limit of rupture is an important part of the model definition since it will exert a first-order control on the ground motions and static offsets. For example, as discussed in section 3, it will determine which parts of the coastline experience subsidence or uplift during a particular event, an important consideration for tsunami hazards. We set the downdip limit to 30 km depth. Analyses of geodetic data, slow-slip events, tremor, and thermal modeling favor shallower downdip limits (~20–25 km) but find that 30 km is a plausible depth [*Frankel et al.*, 2015]. For the synthetic waveforms we choose the locations of 64 currently operating GNSS sites in the U.S. and Canada (Figure 1) that are contributing to geodetic-based EEW algorithms in the Pacific Northwest [*Crowell et al.*, 2016]. This is simply for demonstration purposes; the number of high-rate GNSS stations in the Pacific Northwest is higher, numbering in the several hundreds.

2.2. Stochastic Slip Distributions: The K-L Expansion

First, a target magnitude for the rupture scenario is determined; in this work these are between M_w8.0 and M_w9.2 with 0.1 magnitude unit spacing. We create 100 scenarios for each magnitude bin for a total of

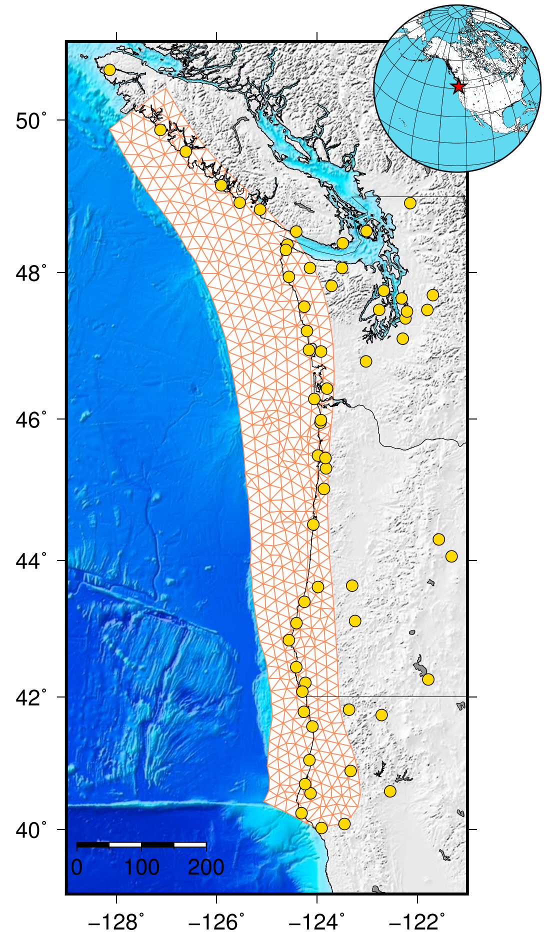

Figure 1. Fault discretization (triangles) and station distribution used for the synthetic data (circles). The downdip limit of the fault model is at 30 km as defined in the Slab 1.0 model for Cascadia [*Hayes et al.*, 2012; *McCrory et al.*, 2012].

1300 events. For a particular realization, once the target magnitude is set, definition of the source properties begins by determining the length, L, and width, W, of the portion of the megathrust (Figure 1) that will participate in rupture. We use the subduction zone rupture dimension scaling laws of *Blaser et al.* [2010]:

$$\begin{aligned} \log_{10}L &= -2.37 + 0.57M_w \\ \log_{10}W &= -1.86 + 0.46M_w \end{aligned}. \tag{1}$$

In order to avoid all events of the same magnitude having the same dimensions, and to introduce some variability, as would be expected in nature, we use a stochastic approach. Equation 3 in *Blaser et al.* [2010] provides the scaling law standard deviations such that one can build a lognormal probability density function of fault lengths and widths and draw random numbers from it. Then, we choose a random subfault to serve as the central locus and apply the scaling-law-derived fault dimensions and select all subfaults within that particular value of L and W. The slab edges are hard boundaries; thus, if the loci are near the edges of the fault model we slide the length and width up or downdip and along strike as necessary until we can fit the randomly drawn dimensions. After determining the subfaults that will be a part of a particular kinematic model the next step is to define the statistics of the slip distribution. We assume that the slip on each patch is normally distributed with mean μ_k and standard deviation σ_k. The vector **s** containing the slips is distributed as

$$\mathbf{s} \sim \mathcal{N}\left(\boldsymbol{\mu}, \hat{\mathbf{C}}\right), \tag{2}$$

where the mean vector $\boldsymbol{\mu}$ is prescribed such that it has uniform slip and enough scalar moment to match the target magnitude. The covariance matrix of the distribution, $\hat{\mathbf{C}}$, is a function of the standard deviation, σ_k, at each subfault, nominally defined as some fraction, typically between 0.5 and 1.0 of the mean slip [*Graves and Pitarka*, 2010], and the correlation C_{ij} between the ith and jth subfaults such that

$$\hat{C}_{ij} = \sigma_i \sigma_j C_{ij}. \tag{3}$$

Thus, the interfault correlation function controls the spatial statistics of slip. It can have many functional forms [*Mai and Beroza*, 2002], but studies have shown that a Von Karman correlation function $C(r)$ best describes the observed slip patterns and is a good choice for ground motion modeling [*Graves and Pitarka,* 2010, 2015; *Mena et al.*, 2010]. The correlation between the ith and jth subfaults is then

$$C_{ij}\left(r_{ij}\right) = \frac{G_H\left(r_{ij}\right)}{G_0\left(r_{ij}\right)}, \tag{4}$$

where

$$G_H\left(r_{ij}\right) = r_{ij}^H K_H\left(r_{ij}\right). \tag{5}$$

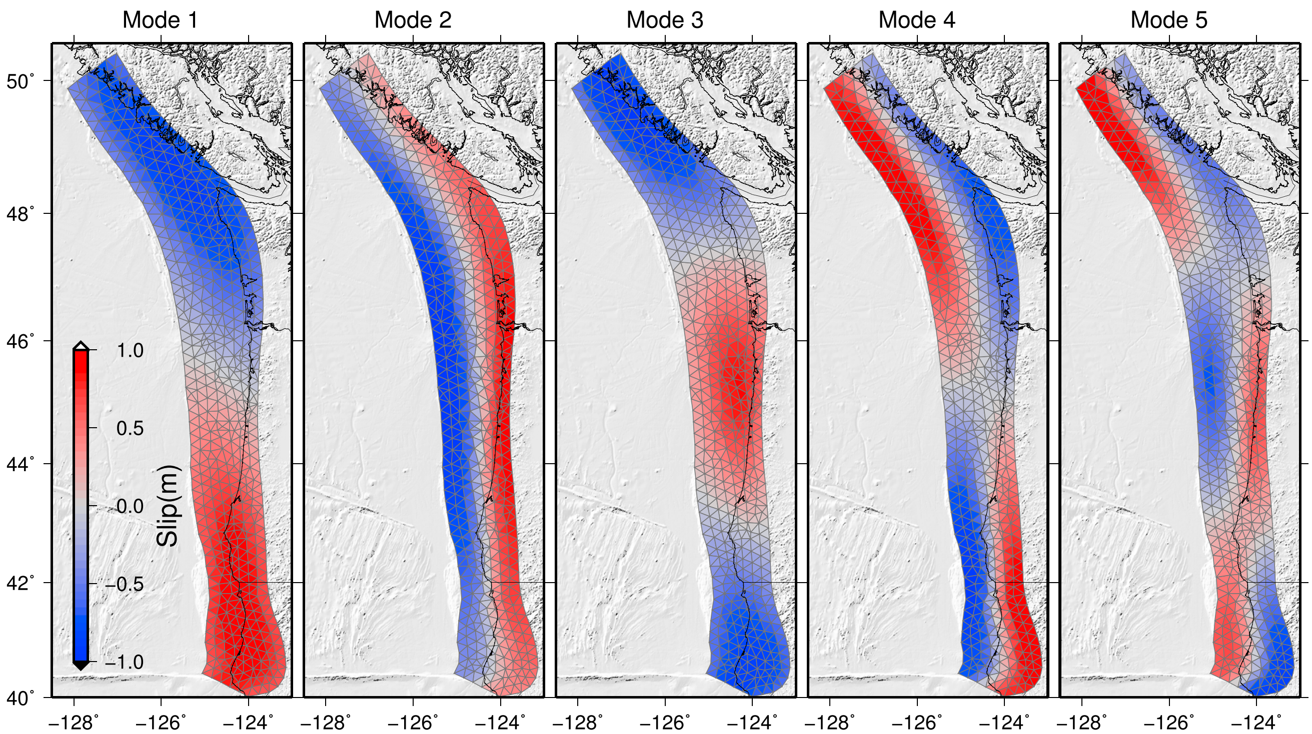

Figure 2. Examples of the first five eigenmodes (ignoring mode 0 which is nearly constant) for a rupture that spans the entire Cascadia megathrust. Each mode is a slip pattern, and the values have been normalized for plotting.

K_H is the modified Bessel function of the second kind (note that *Mai and Beroza* [2002] erroneously called this the modified Bessel function of the first kind), H is the Hurst exponent, and r_{ij} is a length measure between the ith and jth subfaults that depends on the along strike, r_s, and along dip distance r_d between subfaults:

$$r_{ij} = \sqrt{\frac{r_s^2}{a_s} + \frac{r_d^2}{a_d}}. \tag{6}$$

For the curved fault geometry the along strike and along-dip distances are determined by following the curved surface of the slab at a given depth (along-strike) and in the downdip direction. Thus, the distances are formally measured on the fault surface. Following *Graves and Pitarka* [2010, 2015] we set $H = 0.75$. Parameters a_s and a_d are the along-dip and along-strike correlation lengths for the event. Conceptually, the correlation lengths determine the predominant size of asperities in the slip model. These scale with the effective length, L_{eff}, and width, W_{eff}, of the fault dimensions from equation (1) [*Mai and Beroza*, 2000, 2002] as

$$\begin{aligned} a_s &= 2.0 + \frac{1}{3} L_{\mathrm{eff}} \\ a_d &= 1.0 + \frac{1}{3} W_{\mathrm{eff}} \end{aligned}. \tag{7}$$

With these correlation lengths computed the $N \times N$ covariance matrix $\hat{\mathbf{C}}$ can be formed by using equations (3)-(7), where N is the number of subfaults selected to satisfy the length and width requirements of equation (1).

Given the eigenvalues λ_k and eigenvectors $\boldsymbol{v}_k$ of the covariance matrix $\hat{\mathbf{C}}$, the Karhunen-Loève expansion states that a random field, in this case the vector of slip at each subfault, $\mathbf{s}$, can be expressed as the linear combination

$$\mathbf{s} = \boldsymbol{\mu} + \sum_{k=1}^{N} z_k \sqrt{\lambda_k} v_k, \tag{8}$$

where the z_k are normally distributed random numbers used as weights to each eigenmode, $\boldsymbol{v}_k$, such that

$$z_k \sim \mathcal{N}(0, 1). \tag{9}$$

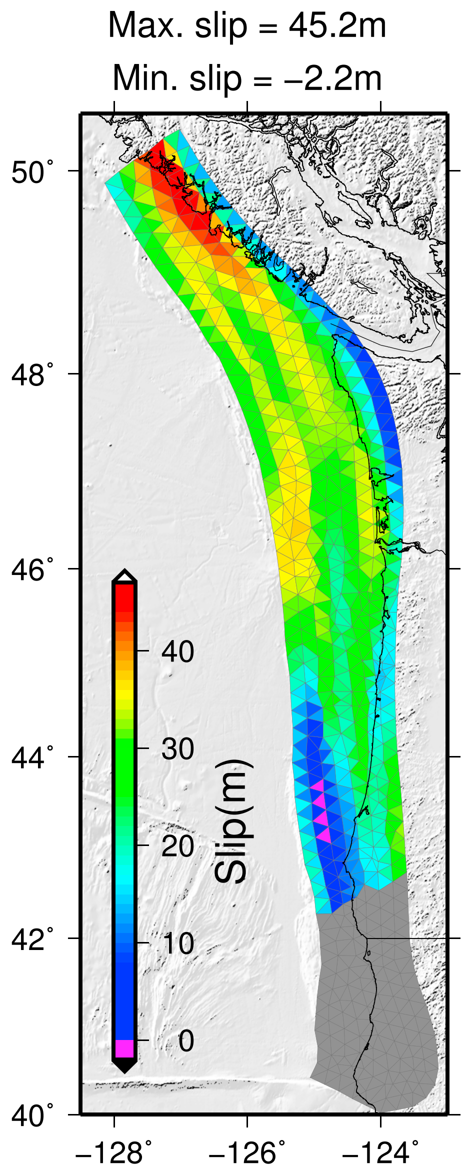

Figure 3. Simulated M_w9.2 ruptures showing negative slip values (magenta) are possible. The grey faults to the south were not selected to participate in rupture given the length and width constraints of equation (1).

Simply by drawing random numbers and forming the linear combination of the eigenmodes of the covariance matrix, one can obtain any number of slip distributions, **s**, that are sampled from a probability density function with the desired covariance $\hat{\mathbf{C}}$ [*LeVeque et al.*, 2016] and thus the correct spatial statistics defined by the modeler. Figure 2 shows the first five modes of the covariance matrix for a M_w9.2 target magnitude event that incorporates all subfaults in the fault geometry. Mode 0, not shown, is roughly constant and does not redistribute slip [*LeVeque et al.*, 2016]; it simply alters the mean. However, the remaining modes have multiple polarity changes and serve to redistribute slip over the fault model. The K-L expansion approach was initially designed by *LeVeque et al.* [2016] for probabilistic tsunami hazard analysis (PTHA). It was shown there that when the eigenvalues decay quickly only a few of the first tens of modes need to be used for long wavelength features and modeling. In the context of PTHA where the quantity of interest is long wavelength in nature, namely, seafloor deformation, *LeVeque et al.* [2016] showed that for the application of generating seafloor deformation for tsunami modeling, a small number of modes often suffices. In this case, however, for kinematic rupture modeling, we are interested in short wavelength variability over the fault. Furthermore, calculation and superposition of the modes are not the heftiest numerical computation in the problem so we do not truncate the K-L expansion.

One difficulty in this formulation is that it is possible for the slip patterns obtained to have both positive and negative slips relative to the defined rake angle. Even when the mean is well above zero, the variability allowed by this stochastic approach can yield a few subfaults with slip values below zero. An example of this is shown in Figure 3. For that example, the four subfaults plotted in magenta have small, compared to the mean, negative values indicating normal faulting within an otherwise thrust fault. It is possible to artificially set these negative slip faults to zero in order to avoid violating nonnegativity. However, depending on the results of the stochastic run, it is possible for a sizable number of the faults to have negative slip. Setting them to zero would then violate the statistical assumptions of the K-L expansion, and no longer ensure that the correlation function assumed (equation (4)) describes the resulting slip pattern. An alternative solution, and the one we employ here, is to use a lognormal distribution that will naturally produce strictly positive results. *LeVeque et al.* [2016] shows that from the previously constructed mean slip $\boldsymbol{\mu}$ and covariance $\hat{\mathbf{C}}$ a log-normally distributed vector of slip can be constructed by defining the mean $\boldsymbol{\mu}^g$ and covariance $\hat{\mathbf{C}}^{\boldsymbol{g}}$ as

$$\begin{aligned} \hat{\mathbf{C}}^g_{ij} &= \log\left(\frac{\hat{\mathbf{C}}_{ij}}{\boldsymbol{\mu}_i\boldsymbol{\mu}_j}+1\right) \\ \boldsymbol{\mu}^g_i &= \log(\boldsymbol{\mu}_i)-\frac{1}{2}\hat{\mathbf{C}}^g_{ii} \end{aligned}. \tag{10}$$

Then the K-L expansion can be applied as before to obtain the new vector

$$\mathbf{s}^g = \boldsymbol{\mu}^g + \sum\nolimits_{k=1}^{N} z_k\sqrt{\lambda^g_k}v^g_k, \tag{11}$$

where the λ^g_k and v^g_k are the eigenvalues and eigenvectors of the covariance in equation (10). Exponentiation will then produce the lognormally distributed slip vector:

$$\mathbf{s} = \exp(\mathbf{s}^g) \tag{12}$$

with mean slip $\boldsymbol{\mu}$ and covariance $\hat{\mathbf{C}}$ This final step ensures a strictly positive slip distribution with the desired spatial statistics. Given enough realizations of the K-L expansion, it is possible to produce slip distributions with what would be considered unrealistically large amounts of slip. Thus, we apply one last geophysical constraint; we place a limit on the peak value of slip. Convergence across the Cascadia subduction zone varies between 35 and 50 mm/yr [*McCaffrey et al.*, 2007], which suggest a slip deficit of ~15 m since the 1700 event. However, it is unknown whether the entirety of the pre-1700 slip deficit was released as coseismic slip during this last large event. Paleo-seismic studies of other subduction zones suggest a complex history of slip accumulation and release [e.g., *Sieh et al.*, 2008]. This is well demonstrated by the 60+ m coseismsic slip during the 2011 M_w9.0 Tohoku-oki earthquake [*Simons et al.*, 2011], which occurred in a region previously thought to have no significant slip deficit. Thus, in an effort to achieve balance between variability in our scenarios and known tectonics we have set the maximum peak-slip limit in our simulations to 60 m, roughly 4 times the expected accumulated slip deficit since the 1700 event. If a particular realization of the K-L expansion exceeds this threshold it is discarded.

2.3. Kinematics

After the slip pattern is obtained we follow *Graves and Pitarka* [2010, 2015] for the kinematic parameters of rupture. We embed the fault in a radially symmetric Earth structure model developed for ground motion analysis by *Gregor et al.* [2002] for the Cascadia subduction zone. We select a random subfault as the hypocenter; rupture onset times are then determined in two stages. First, we assume a background rupture speed (v_r) distribution where

$$v_r = \begin{cases} 0.56 \times v_s \ ; \ d < 10 \ \text{km} \\ 0.80 \times v_s \ ; \ d > 15 \ \text{km} \end{cases}. \tag{13}$$

Parameter v_s is the local shear-wave speed model, d is the depth of the subfault centroid, and a linear transition in rupture speed is applied between 10 and 15 km depth. This reduction in rupture speed at the shallow megathrust is justified from observations of large events and back-projection studies [*Lay et al.*, 2012]. The onset times from this background distribution are then perturbed in the same way as *Graves and Pitarka* [2010] to allow for faster propagation where slip is large and slower where slip is small.

The duration of slip (the risetime) at each subfault, T_i, is scaled by the square root of the total slip at the subfault

$$T_i = \begin{cases} 2ks_i^{1/2} \ ; \ d < 10 \ \text{km} \\ ks_i^{1/2} \ ; \ d > 15 \ \text{km} \end{cases}, \tag{14}$$

where the constant k is chosen such that the average risetime over the entire fault, T_a, is equal to the empirically determined value given by *Somerville et al.* [1999]

$$T_a = 4.308 \times 10^{-7} \times \mathrm{M}_0^{1/3}, \tag{15}$$

where $\mathbf{M}_0$ is the scalar moment in N-m, and we have modified the constants from the original relationship in *Somerville et al*. [1999], which was given in dyne-cm. With this scaling larger amounts of slip will take longer risetimes. As noted by *Graves and Pitarka* [2010] this scaling represents a compromise between the two end-member scenarios of constant risetime and constant slip velocity. The elongation of risetimes at shallow depths in equation (14) is also justified by observation of large events [*Lay et al.*, 2012]. This effect is particularly obvious for the 2011 M_w 9 Tohoku-oki event where source time functions in slip inversions are notably longer for shallow subfaults [e.g., *Melgar and Bock*, 2015]. For continental faults *Graves and Pitarka* [2015] employ a second depth-dependent modification and elongate the risetimes of deep subfaults as they approach the brittle/ductile transition. We have not added this to our simulations. In subduction zone environments teleseismic back projection has shown clear segregation of low- and high-frequency radiators between the shallow and deep portions of the megathrust [e.g., *Kiser and Ishii,* 2012; *Melgar et al.*, 2016b]. Furthermore, it has been observed that strong motions are preferentially generated in the deeper part of the megathrust with the high-frequency radiators and short risetimes [*Kurahashi and Irikura*, 2011]. By neglecting this second depth-dependent risetime elongation effect we hope to capture this behavior.

Finally, slip must be parameterized by a local slip-rate function. We depart from *Graves and Pitarka* [2010, 2015] by choosing the Dreger slip-rate function [*Mena et al.*, 2010] defined as

$$\dot{s}_i(t) = t^{-\varsigma} e^{-t/4\tau}, \tag{16}$$

where $\zeta = 0.2$ and the local risetime is $T_i = 4\tau$. Other popular choices are isosceles triangles, the regularized Yoffe function [*Tinti et al.*, 2005], and the cosine function [*Liu et al.*, 2006]. These suffer from two shortcomings; they have spectral notches and a high-frequency (f) decay proportional to f^{-2} (see section 5). The f^{-2} decay is problematic because the effective moment rate is a combination of the slip velocity function and the finite-rupture terms governed by the slip and rupture velocity distribution. Thus, slip velocity functions with f^{-2} decay will result in a net high-frequency decay rate that can be significantly greater (as high as f^{-3}). The Dreger slip-rate function has a continuous spectrum with high-frequency decay rate that is a function of ζ. Small values of ζ, such as $\zeta = 0.1$ or $\zeta = 0.2$, yield a high-frequency falloff rate close to f^{-1} consistent with theory [*Mena et al.*, 2010]. Thus, the advantage of this slip rate function is that ζ can be adjusted such that the spectral shape, especially the high-frequency falloff rate, fits the f^{-1} constraint for any given finite-rupture model.

2.4. Waveform Synthesis

Once the slip distribution and the kinematic properties are defined we use an elastodynamic Green's function (GF) matrix multiplication approach to synthesize waveforms at the selected stations (Figure 1). Impulse responses are computed by using a frequency-wave number integration algorithm [*Zhu and Rivera*, 2002] for every subfault/station pair and each of the three components of motion (east, north, and vertical) from the static offset to a maximum frequency of 1 Hz. For each one of the 1300 scenario ruptures determined by using the approach of sections 2.2 and 2.3 we retrieve the appropriate risetimes, create the associated slip-rate functions for each subfault (equation (16)), and scale it such that its integral produces the correct amount of slip. This is then convolved with the impulse response and delayed by the appropriate rupture onset time. Subsequently, it is added to the GF matrix. Once the GF matrix is fully formed multiplication by the model vector of slips, **s**, yields the three-component waveforms at each site.

3. Results

Figure 4 shows four representative slip distributions from the catalogue of 1300 scenario events. They illustrate some of the built in variability in the method; for example, peak slip is larger for the M_w8.66 event than for the M_w8.91 event; however, the M_w8.91 has a substantially longer length and a larger area of high slip. The scenarios also illustrate the two factors contributing to risetime scaling; patches of large slip have longer risetimes than do shallow patches. The variability in onset times is also well illustrated in these examples. Rupture propagates faster at depth in the portions of the Earth model with higher shear wave speed; these examples also show faster propagation speed in areas of large slip.

The behavior of all 1300 scenarios is summarized in Figure 5. The variability in the length and width around the mean defined by the *Blaser et al.* [2010] scaling law (equation (1)) is depicted in Figures 5a and 5b. The width saturates, given our choice of a downdip edge of slip, roughly for M_w8.6 and larger. The mean slip and risetimes are more or less constant for any given magnitude; however, their maximum values and scatter, illustrated by the standard deviations, vary substantially between events. We note that there are differences

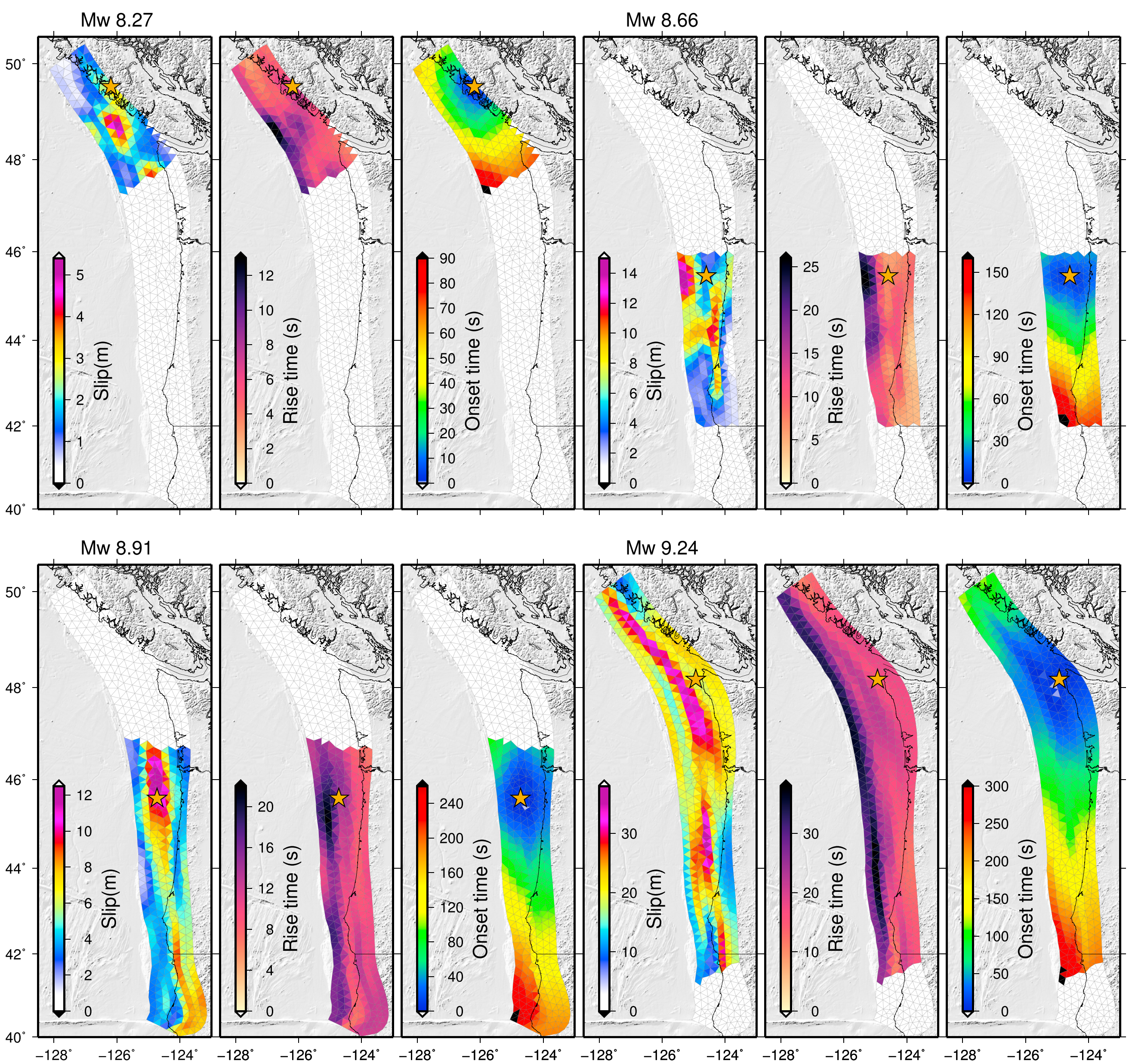

Figure 4. Sample scenarios. Plotted are the slip, risetimes, and onset times for each scenario. The star denotes the position of the hypocenter.

between the target and actual magnitudes in the resulting models. This is due to the stochastic nature of the method; the target magnitude constrains the mean slip used a priori (equation (10)) but after the stochastic process there is no requirement that the final moment matches the target moment. There is a parameter in the code that will rescale the slip pattern to match the target moment exactly; however, we have not used it in the simulations shown here.

An example of the synthesized waveforms can be seen in Figure 6, where all the waveforms for the M_w8.66 scenario are plotted. The superposition of strong shaking ($f < 1$ Hz), at the close in stations, with permanent deformation is particularly obvious in the east component, where, as expected for an eastward dipping thrust fault, there is substantial westward motion. Interestingly, at stations with substantial static offsets, where near and intermediate field terms still contribute, we observe that the static offset begins its growth in between the P and S wave arrivals. At the further afield stations the records are dominated by surface waves. A close-up of this is shown in Figure 7, where three stations for the same M_w8.66 event of Figure 4 are plotted

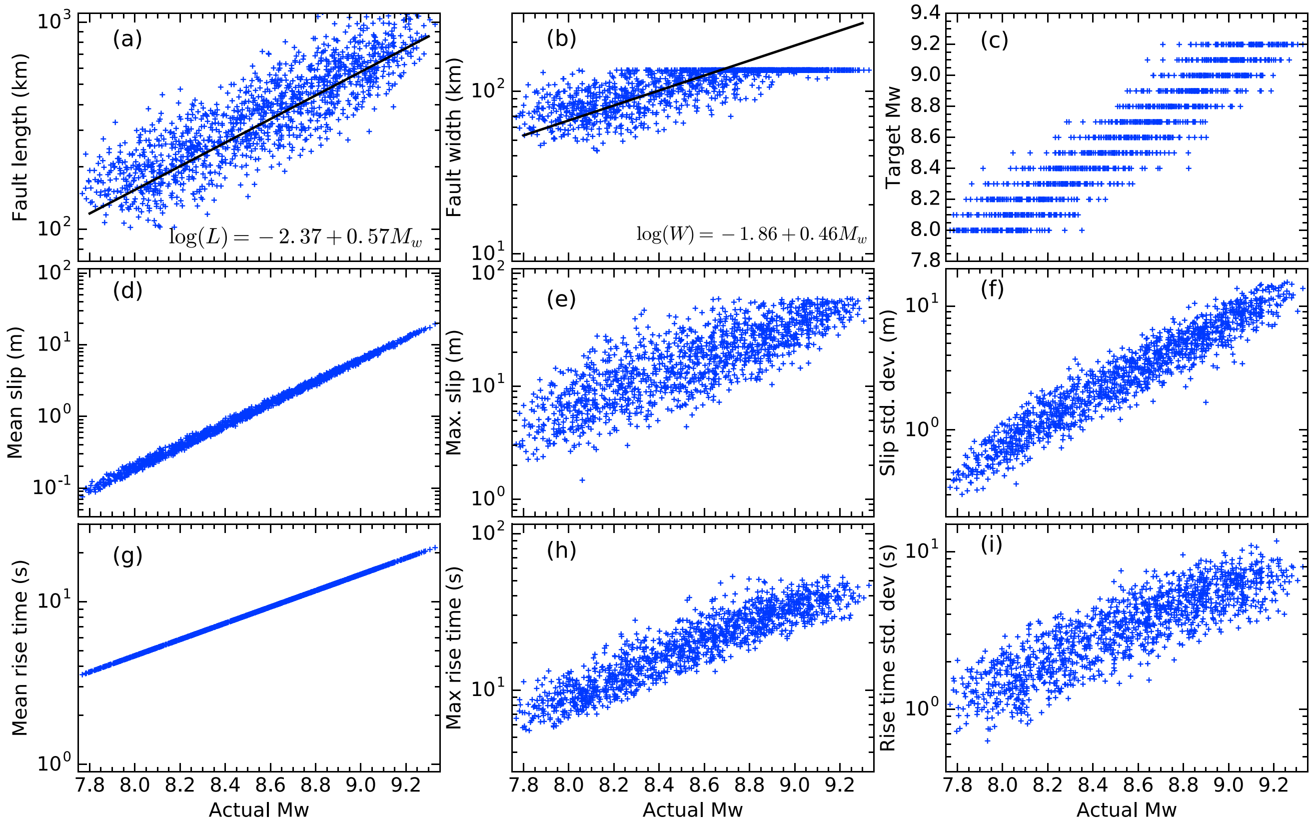

Figure 5. Summary statistics for the 1300 scenario events. (a and b) The length and width distributions compared to the scaling laws of *Blaser et al.* [2010]. Note that the width saturates due to our selection of 30 km as the downdip depth of slip. (c) The comparison between the target magnitude for a given event and the final simulated or "actual" magnitude. (d–f) The mean, maximum, and standard deviation of slip. (g–i) The mean, maximum, and standard deviation of the risetimes.

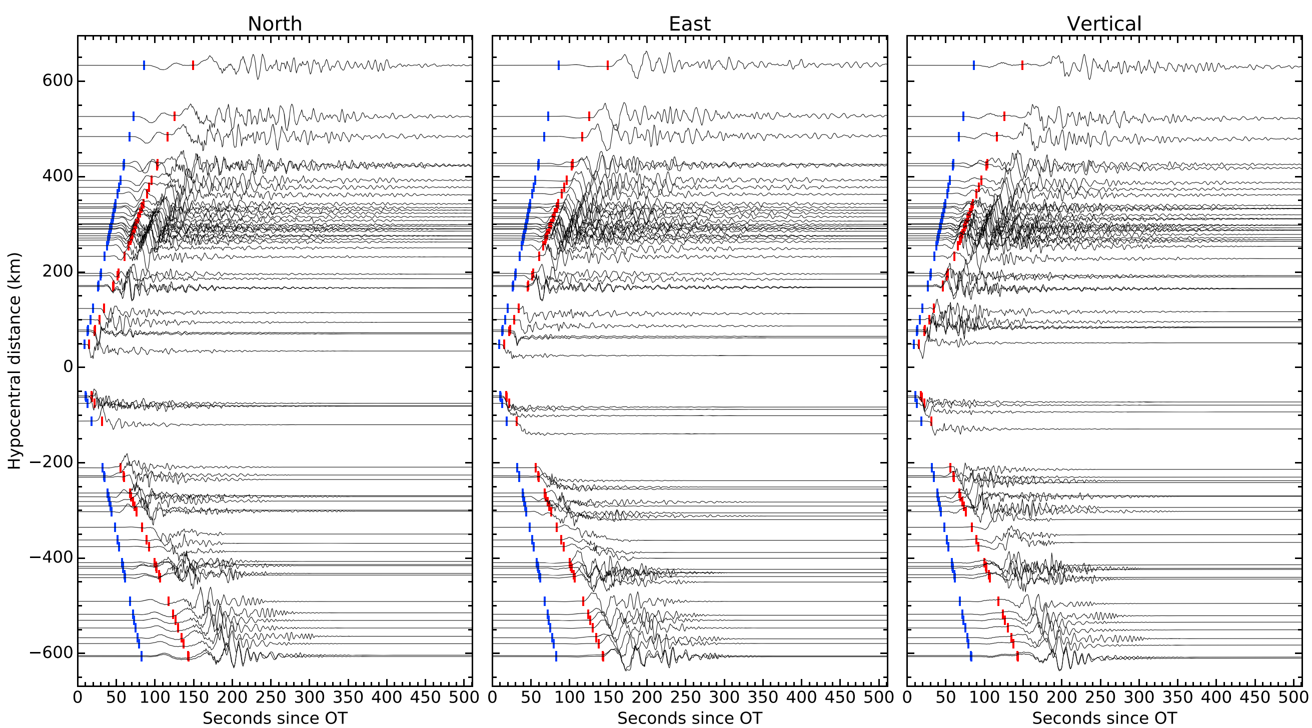

Figure 6. Record section for the M_w8.66 event in Figure 4. The waveform amplitudes are normalized for clarity. The blue and red hashes are the *P* and *S* wave arrival times independently computed by ray-tracing through the Earth structure model.

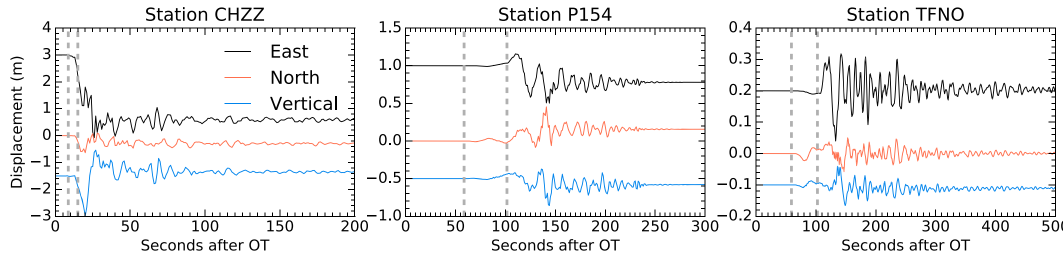

Figure 7. Close-ups of the waveforms for three stations in the record section of Figure 6. The dashed lines are the *P* and *S* wave arrivals determined from ray-tracing. The waveforms are offset for clarity.

at varying hypocentral distances. As noted previously, the synthesized waveforms capture the static offsets well (Figure 8) and the results show the complexity of the coseismic deformation field, with the coastal stations showing uplift or subsidence depending on their relative position to large patches of slip. Capturing this behavior is important if the scenarios are to be useful for assessing tsunami hazards as well. The vertical motion of coastline features can have a substantial impact on tsunami intensities.

4. Validation

Synthetic ground motions are typically validated by comparison to empirically derived GMPEs [e.g., *Dreger et al.*, 2015; *Goulet et al.*, 2015]. As noted in section 1 GMPEs relate acceleration and velocity ground motion parameters to source properties and source/station distances. Displacement parameters are not usually included due to difficulties in processing strong motion data to obtain displacements [*Boore and Bommer*, 2005]. Recently, there have been efforts to quantify the source scaling properties of displacement ground motions measured directly by GNSS. *Crowell et al.* [2013] first noted that peak ground displacement measured by GNSS stations, consisting of the superposition of the static offset and strong shaking, scaled as a function of the source properties. *Melgar et al.* [2015] calculated a PGD GMPE and scaling law for 10 events recorded by GNSS spanning M_w 6–9. We rely on direct comparison to this scaling law to assess the quality of the simulations; it is

$$\log(\mathrm{PGD}) = -4.434 + 1.047M_w - 0.138M_w \log(R), \quad (17)$$

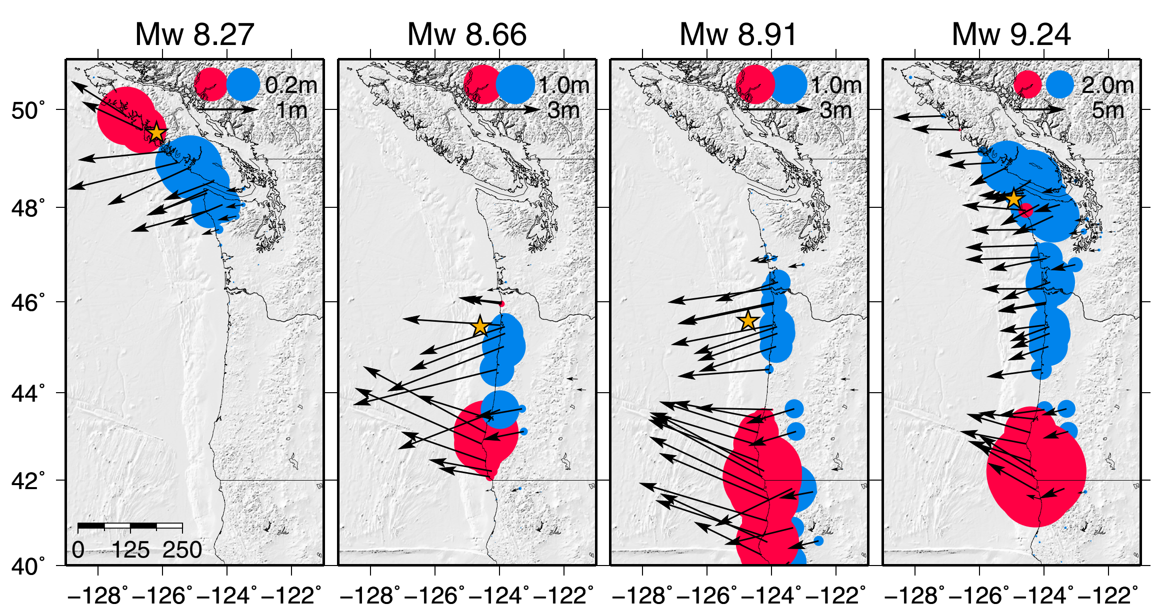

Figure 8. Coseismic offsets at modeled stations for the four sample events from Figure 4. The arrows indicate the horizontal offsets, while the blue and red circles indicate the subsidence and uplift, respectively. The star is the event hypocenter.

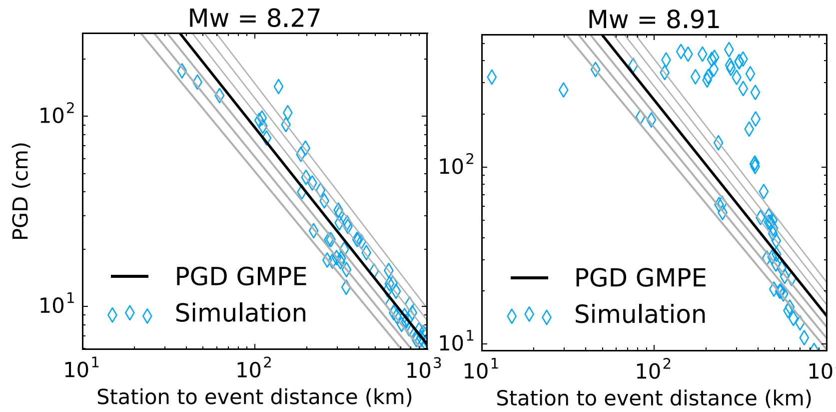

Figure 9. Example comparison between the PGD values from two of the simulated events (blue diamonds) on Figure 4 and the PGD values (black line) predicted by the relationship of *Melgar et al.* [2015] for a given magnitude. The grey line indicates the predicted values for ±0.3 magnitude units from the event magnitude.

where log() denotes base 10 logarithm and R is the source to station distance where we use the moment centroid of the fault model as the source reference point. Figure 9 shows the comparison between the predicted PGD values and those observed in the simulations for two of the events in Figure 4. Overall, they match well but the example illustrates a pervasive feature; smaller magnitude events are very well fit by the GMPE with the misfit increasing at larger magnitudes. To systematically assess the differences between the simulated PGDs and the predictions of equation (17) we define the residual at each site i

$$\rho_i = \ln\left(\frac{\mathrm{PGD}_{\mathrm{simulated},i}}{\mathrm{PGD}_{\mathrm{GMPE},i}}\right). \tag{18}$$

A positive residual indicates that the simulations produce PGDs larger than what is expected from the GMPE and a negative residual that the simulation underpredicts PGD. The residuals for all stations and events as a function of source to station distance are grouped into 20 magnitude and 30 distance bins. *Dreger et al.* [2015] noted that in order to avoid bin-dependent bias a good combined goodness of fit metric (CGOF), as a function of the residuals ρ_i, is

$$\mathrm{CGOF} = \frac{1}{2}|\langle \rho_i \rangle| + \frac{1}{2}\langle |\rho_i| \rangle, \tag{19}$$

where $\langle\rangle$ denotes the mean and $||$ denotes the absolute value. Figure 10 shows the mean values for the residuals in each magnitude/distance bin as well as the value of CGOF in each bin. The number of simulated

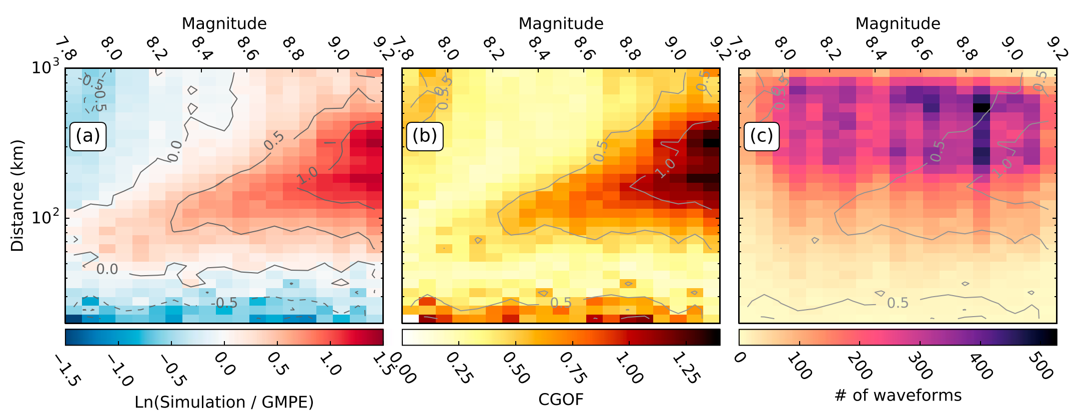

Figure 10. (a) Residuals (equation (18)) as a function of distance and magnitude. (b) Combined goodness of fit (CGOF; equation (19)) as a function of distance and magnitude. (c) Number of waveforms in each distance/magnitude bin. The contours are the CGOF values from Figure 10b.

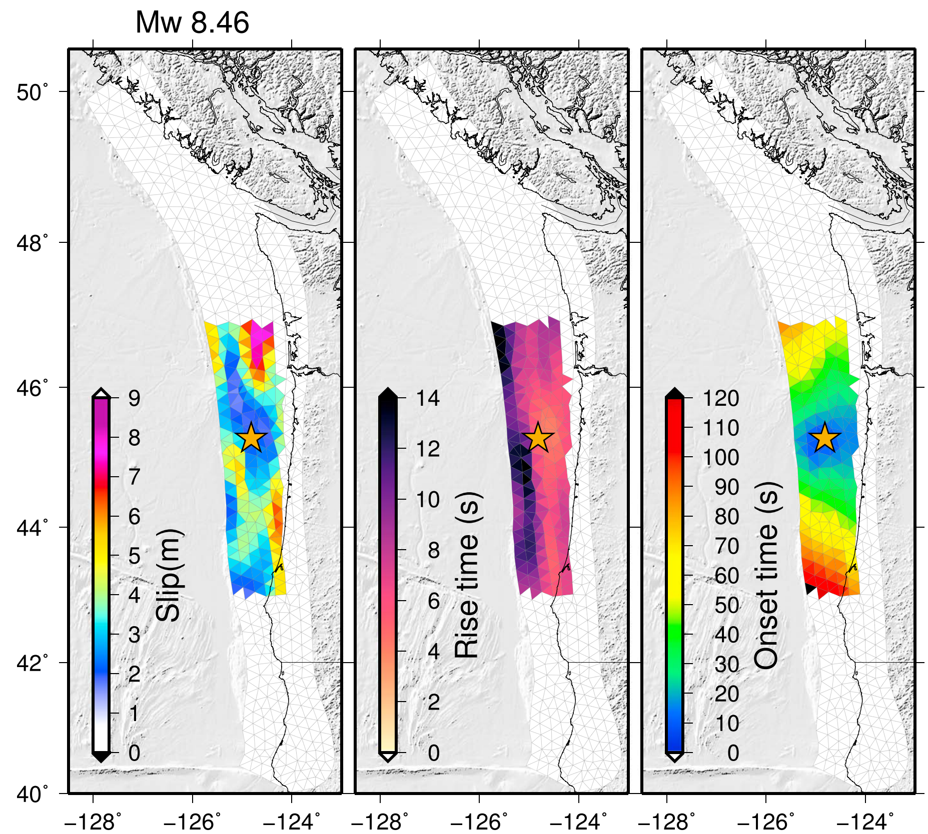

Figure 11. Example scenario where the downdip limit of rupture is not reached.

waveforms in each bin is also plotted. Any hard limit on what is an acceptable level of misfit is inherently subjective; however, *Dreger et al.* [2015] suggested that a value of CGOF < 0.7 is a good limit for an acceptable fit. In that context, a large majority of the waveforms are in bins with good fits. However, we also note that the fits to the PGD GMPE systematically degrade as the magnitudes get larger as was noted with Figure 9. This likely reflects shortcomings of the simple GMPE we have used for validation. It lacks the complex terms of most GMPEs such as hanging wall effects, other measures of source/station distance, directivity, and site conditions [*Boore et al.*, 2014].

5. Discussion

The results shown demonstrate how the K-L expansion method can be used to produce realistic slip distributions. These can be combined with previous work on ground motion modeling to generate kinematic ruptures and simulate GNSS waveforms. In Figure 4 we showed four examples of slip distributions produced in this way. However, as further shown in Figure 5 there is significant variability in the 1300 scenario events we created. We consider this a strength of the method. The goal of this approach is to generate synthetic ruptures and waveforms that capture, not what is most likely, but what is possible. For example, *Frankel et al.* [2015] summarized the inferred downdip edges of slip from several studies and their potential effect on ground motion, from those results we have chosen a deep, but probable 30 km depth as the downdip edge. This has an impact on the vertical deformation of the coastline (Figure 8). Roughly, south of 45°N, where the continental shelf is short, a substantial portion of the slip in the examples of Figure 4 happens onshore. This leads to uplift of the coastline. It is markedly different from the situation on the northern portion of the subduction zone where subsidence is far more prevalent than uplift due to the wider shelf. This will have an effect on assessment of the tsunami hazard. However, given the variability built into our method events that do not reach this downdip limit occur naturally, an example M_w8.46 event is shown in Figure 11.

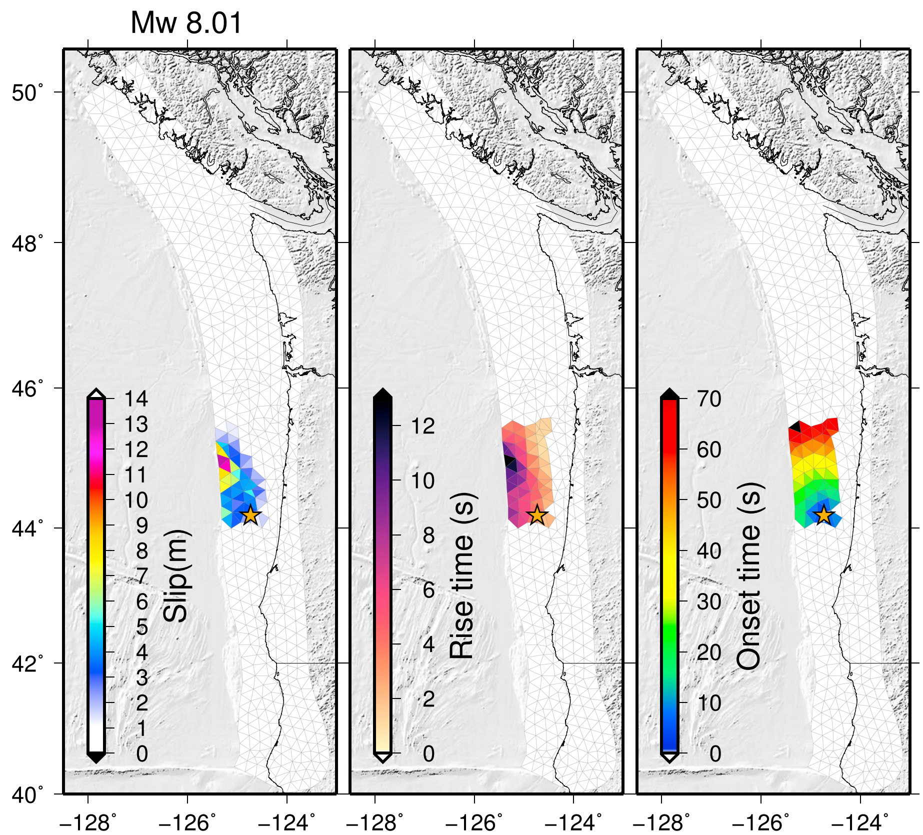

Figure 12. Example of a *tsunami* event. This earthquake has very large slip and long risetimes on the shallow portion of the megathrust.

Similarly, because of the depth-dependent risetime scaling we have employed, *tsunami events* are generated and are a part of the scenario ruptures. These are earthquakes with substantial shallow slip, slow rupture, and long risetimes, which do not efficiently generate strong motions but easily produce sizable tsunamis [e.g., *Hill et al.*, 2012], Figure 12 shows an example of a M_w8.01 tsunami event. Additionally, extreme events are also a part of the suite of scenario ruptures. Consider Figure 13 where we show two examples. The M_w8.78 earthquake depicted has one narrow asperity with large peak slip (~30 m). According to the fault length scaling law of equation (1) a M_w8.78 rupture is expected to have a length of ~430 km; however, this event concentrates the majority of its slip over a length of ~100 km. The M_w8.9 in Figure 13 shows the opposite kind of extreme behavior; at M_w8.90 its length is expected to be ~500 km; however, this event spans more than 1000 km of the subduction zone with large swaths of the slip distribution having relatively small amounts of slip. Events such as these are outliers, but if enough simulations are run they are seen to occur. These are a few examples of what is in the suite of scenarios we have generated, and it is possible to have learned debates on the likelihood of many of them; however, there are sufficient tunable parameters in our approach that, should a particular modeler, want to temper the variability it could be done, and more commonly observed events could be produced. For example, *Goldfinger et al.* [2012] have suggested, based on turbidite records, that large ruptures in Cascadia are segmented and occur predominantly on two distinct patches. Such geologic constraints can be easily enforced in our scenario generation, for example, by limiting the large events with $M_w < 8.7$ to exclusively rupture on the northern or southern part of the fault and have the very large events rupture on the entire slab model. By design, our method has enough flexibility that modeling decisions can be made and implemented to fit the criteria and goals of any particular study. Nonetheless, other than the downdip edge of rupture, in the examples discussed in this paper, we have not enforced any other geologic constraints. This design philosophy is driven by the fact that given the long recurrence times, only a few large events have been observed worldwide in the time of instrumental seismology and

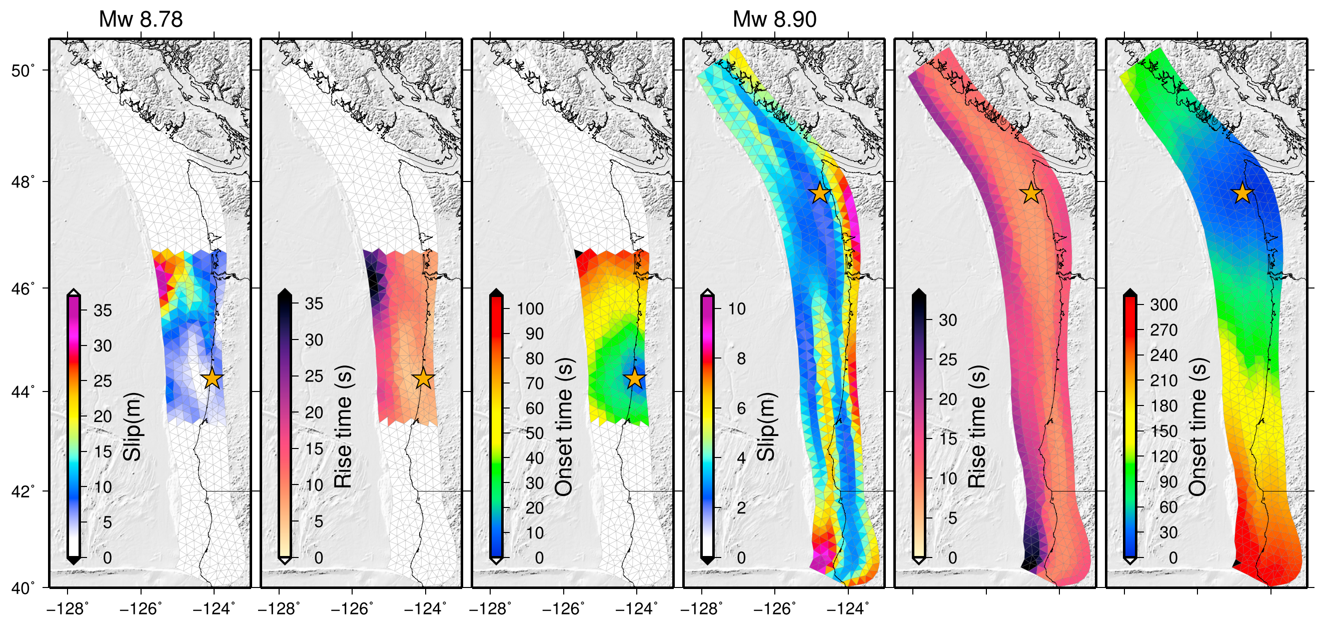

Figure 13. Examples of extreme events. Plotted are two examples, on event with very large slip over an area much smaller than what is predicted by the scaling laws of *Blaser et al.* [2010]. The second event has comparatively smaller amounts of slip over an area much larger than what is predicted by the scaling laws.

geodesy, and none in Cascadia. The uncertainties of the inferred source parameters from paleoseismic studies are inherently large, and therefore, there is good reason to explore scenarios that challenge preconceptions of what is likely.

Broadband ground motion simulation has typically meant generating and validating waveforms with spectral content in the 0.1–50 Hz range [e.g., *Liu et al.*, 2006; *Graves and Pitarka*, 2010; *Mena et al.*, 2010]. When considering velocity and acceleration ground motion metrics this frequency range is sufficient. However, for modeling displacements from large ruptures the long-period band has to be extend to 0 Hz in order to capture not just the static offset but the substantial long-period ground motions which dominate displacement records [*Melgar et al.*, 2013]. *Kamai and Abrahamson* [2015] showed how metrics such as PGD are underestimated and generally not well captured by modern GMPEs. Thus, for validation, we have relied on what is, to our knowledge, the only displacement-based GMPE directly derived from GNSS measurements of large earthquakes [*Melgar et al.*, 2015]. Following the validation framework discussed in *Dreger et al.* [2015], we argue that our simulated waveforms compare favorably to this PGD scaling law. However, we recognize that the pattern of the misfits to the GMPE (Figure 10) shows a systematic degradation for the largest magnitude events. This likely reflects shortcomings of the simple PGD GMPE we have compared our simulations to, which assumes a point source (equation (17)) and lacks many of the more complex terms of most GMPEs such as hanging wall effects, other measures of source/station distance, directivity, and site conditions [*Boore et al.*, 2014]. Using better distance metrics such as the Joyner-Boore minimum surface fault projection distance (R_{jb}) in the GMPE regression will likely lead to substantial improvements. Consider Figures 4 and 9, for the M_w8.91 event it is clear that using the station to centroid distance as a metric gravely affects the prediction of PGD for the close in stations. *Dreger et al.* [2015] in another validation exercise noted that for layered models surface waves are efficiently trapped and lead to over estimation of ground motions, and it is possible that this is also the case here. Nonetheless, we contend that the favorable comparison to the GMPE, in spite of its simplicity, is indicative of the reliability of the simulated waveforms. More work is needed to understand and extend the contributions of GNSS recorded long-period strong motions to GMPEs, particularly to displacement based intensity measures such as PGD. While many of the familiar tools of ground motion prediction will carry over, other aspects of PGD are fundamentally different. For example, higher-frequency metrics such as PGA and PGV are seen to saturate with magnitude [*Brune,* 1970; *Baltay and Hanks*, 2014]; no such saturation effect is seen in the PGD data collected; thus far [*Melgar et al.*, 2015], nor is it expected to, slip scales directly with moment and the main contribution to PGD is the static offset, which itself should grow as moment, and thus slip, increases.

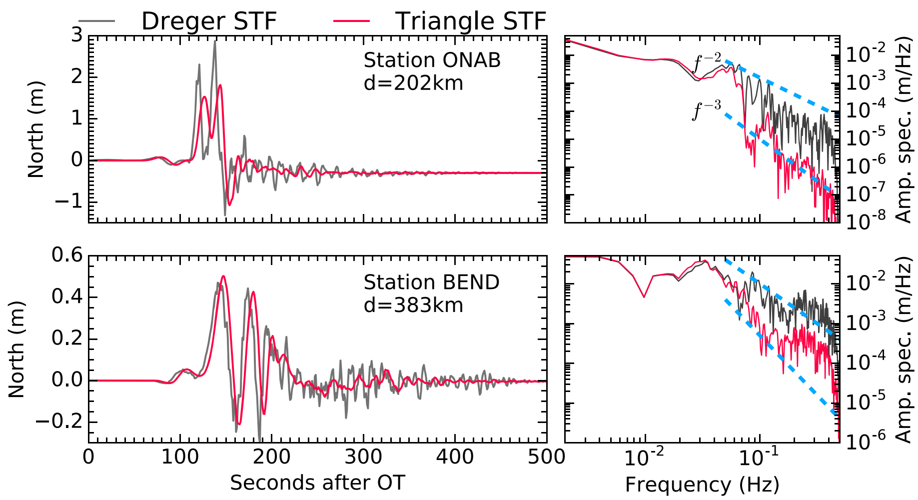

Figure 14. Dreger and triangle slip rate functions using the average risetime of 21.1 s for the M_w9.24 event of Figure 4. The spectra show a high-frequency decay rate proportional to f^{-1} for the Dreger function and f^{-2} for the triangle function. Also visible are the spectral notches in the triangle function.

Even though in this work we focus on simulating long-period ground motions we find that the choice of parameterization of the source time function can have an effect on the results. *Mena et al.* [2010] noted that compared to other common choices such as the regularized Yoffe, cosine, and triangle source time functions (STFs), the Dreger STF has the f^{-1} high-frequency decay compatible with what is expected from theoretical considerations, compared to the more rapid f^{-2} decay from the other slip velocity functions. This is exemplified in Figure 14, we have taken the average risetime (21.1 s) for the M_w9.4 earthquake of Figure 4 and plotted the corresponding Dreger and triangle slip-rate functions and their amplitude spectra. The substantially faster high-frequency falloff rate of the triangle STF and the spectral notches are clearly visible. This faster high-frequency decay in the triangle STF, when convolved with the finite-rupture process, yields an artificially high-frequency falloff in the synthesized waveforms. Figure 15 plots the east component waveforms for two stations for the M_w8.91 event in Figure 4. We plot the results for the Dreger and triangle STF. While both waveforms converge to the same static offset there are appreciable differences at the higher frequencies. We also show in Figure 15 the amplitude spectra of Dreger STF-derived and triangle STF-derived waveforms. They clearly show that, for this example, at periods shorter than the corner frequency defined by the average risetime (~0.05 Hz) the Dreger STF waveform has substantially more spectral content.

One important field where our results can be applied is in the testing and evaluation of earthquake and tsunami early warning systems. For EEW many of the geodesy-based algorithms [*Ohta et al.*, 2012; *Grapenthin*

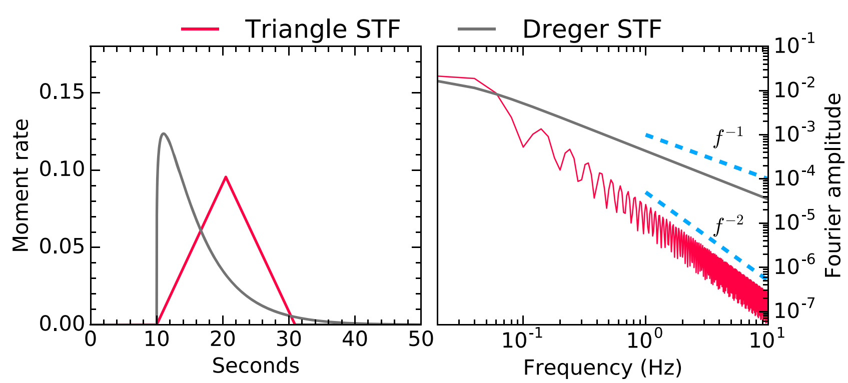

Figure 15. Effect of the choice of source time function. The waveforms are for the M_w9.24 event in Figure 4 at 202 km and 383 km from the slip centroid. They were calculated by using the Dreger STF and the triangle STF. The amplitude spectra show the deficiency in high-frequency content when using the triangle STF.

et al., 2014; *Minson et al.*, 2014; *Crowell et al.*, 2016] can be routinely tested to identify weaknesses and assess their performance. An important area of future work will be to expand the results from this work to higher frequencies and truly broadband ground motion simulations. Most of the aforementioned approaches that use GNSS for EEW rely on triggers from seismic-based algorithms that utilize ground motion parameters from higher frequency data (~1-10Hz). Then, for a truly end-to-end test of the performance of these seismic/geodetic coupled systems modeling higher frequencies with hybrid deterministic/stochastic methods [*Dreger and Jordan*, 2015] will be important. Similarly, for tsunami early warning having access to a framework that can easily produce synthetic slip distributions should be useful to assess the performance of propagation models. Tsunami warning systems are embracing GNSS data as a source of rapid information on the earthquake source that can be used to determine tsunami sources and launch propagation models [*Melgar et al.*, 2016a]. With synthetic waveforms such as those produced here, it will be possible to assess the reliability and uncertainties in local warnings produced by using GNSS techniques.

6. Conclusions

We have demonstrated an approach to generating synthetic long-period displacement waveforms at the sampling rate of traditional GNSS networks. We expect that methods such as this can be used for earthquake and tsunami hazard assessment and for testing the performance of earthquake and tsunami warning algorithms that rely on GNSS data as their main source of input. We have shown an application of the Karhunen-Loève expansion to generate stochastic slip distributions with an example application to the Cascadia subduction zone. We have also shown a method to expand the K-L expansion-derived slip distributions to produce kinematic rupture models and generate synthetic GNSS data. We validated the waveforms produced by our method with a displacement-based GMPE based on peak ground displacement measurements from GNSS measurements of large earthquakes. We note that it remains challenging to validate displacement synthetics, especially for larger (~*M*9) events, due to the primitive state of displacement-based GMPEs. However, we have relied on a simple PGD GMPE to validate the waveforms and found good agreement. We note that a prominent area of future research will be to incorporate GNSS-derived measurements of strong motion displacements into the mainstream framework of GMPEs.

Finally, we note that the code used to generate the scenario slip distributions and waveforms is freely available to the community (see the Acknowledgments section), and the slip distributions, model definitions, and waveforms are part of the supporting information.

Acknowledgments
This work was funded in part by the USGS grants G15AC00081, G15AC00331, and G15AP00087. At UW this work was funded by the NSF grants DMS-1216732 and EAR-1331412 and the FEMA contract EMW-2014-CA-00218-S01. The FakeQuakes module used to generate the slip distributions is part of the MudPy suite of source modeling and inversion codes and can be obtained at http://www.github.com/dmelgarm/MudPy. Waveforms and supporting files for all simulations can be found on Zenodo at https://zenodo.org/record/59943. We would like to thank Christine Ruhl for a careful reading of the revised manuscript.

References

Allen, R. M., P. Gasparini, O. Kamigaichi, and M. Böse (2009), The status of earthquake early warning around the world: An introductory overview, *Seismol. Res. Lett.*, *80*(5), 682–693.

Baltay, A. S., and T. C. Hanks (2014), Understanding the magnitude dependence of PGA and PGV in NGA-West 2 data, *Bull. Seismol. Soc. Am.*, *104*(6), 2851–2865.

Blaser, L., F. Krüger, M. Ohrnberger, and F. Scherbaum (2010), Scaling relations of earthquake source parameter estimates with special focus on subduction environment, *Bull. Seism. Soc. Am.*, *100*, 2914–2926.

Bock, Y., and D. Melgar (2016), Physical applications of GPS geodesy: A review. *Rep. Prog. Phys.*, *79*(10), 106801, doi:10.1088/0034-4885/79/10/106801.

Boore, D. M., and J. J. Bommer (2005), Processing of strong-motion accelerograms: Needs, options and consequences, *Soil Dynam. Earthquake Eng.*, *25*(2), 93–115.

Boore, D. M., J. P. Stewart, E. Seyhan, and G. M. Atkinson (2014), NGA-West2 equations for predicting PGA, PGV, and 5% damped PSA for shallow crustal earthquakes, *Earthquake Spectra*, *30*(3), 1057–1085.

Brune, J. N. (1970), Tectonic stress and the spectra of seismic shear waves from earthquakes, *J. Geophys. Res.*, *75*, 4997–5009, doi:10.1029/JB075i026p04997.

Crowell, B. W., D. Melgar, Y. Bock, J. S. Haase, and J. Geng (2013), Earthquake magnitude scaling using seismogeodetic data, *Geophys. Res. Lett.*, *40*, 6089–6094, doi:10.1002/2013gl058391doi:10.1002/2013gl058391.

Crowell, B. W., et al. (2016), Demonstration of the Cascadia G-FAST geodetic earthquake early warning system for the Nisqually, Washington earthquake, *Seismol. Res. Lett.*, doi:10.1785/0220150255.

Dreger, D. S., and T. H. Jordan (2015), Introduction to the focus section on validation of the SCEC broadband platform v14. 3 simulation methods, *Seismol. Res. Lett.*, *86*(1), 15–16.

Dreger, D. S., G. C. Beroza, S. M. Day, C. A. Goulet, T. H. Jordan, P. A. Spudich, and J. P. Stewart (2015), Validation of the SCEC broadband platform v14. 3 simulation methods using pseudospectral acceleration data, *Seismol. Res. Lett.*, *86*(1), 39–47.

Frankel, A., R. Chen, M. Petersen, M. Moschetti, and B. Sherrod (2015), 2014 Update of the Pacific Northwest Portion of the US National Seismic Hazard Maps, *Earthquake Spectra*, *31*(S1), S131–S148.

Goldfinger, C., et al. (2012), Turbidite event history—Methods and implications for Holocene paleoseismicity of the Cascadia subduction zone: U.S, Geological Survey Professional Paper 1661–F, 170 p.

Goulet, C. A., N. A. Abrahamson, P. G. Somerville, and K. E. Wooddell (2015), The SCEC Broadband Platform Validation Exercise: Methodology for code validation in the context of seismic-hazard analyses, *Seismol. Res. Lett.*, *86*(1), 30–45.

Grapenthin, R., I. A. Johanson, and R. M. Allen (2014), Operational real-time GPS-enhanced earthquake early warning, *J. Geophys. Res.: Solid Earth*, *119*, 7944–7965, doi:10.1002/2014JB011400.

Graves, R., and A. Pitarka (2015), Refinements to the Graves and Pitarka (2010) broadband ground-motion simulation method, *Seismol. Res. Lett.*, *86*(1), 75–80.

Graves, R. W., and A. Pitarka (2010), Broadband ground-motion simulation using a hybrid approach, *Bull. Seismol. Soc. Am.*, *100*, 2095–2123.

Gregor, N. J., W. J. Silva, I. G. Wong, and R. R. Youngs (2002), Ground-motion attenuation relationships for Cascadia subduction zone megathrust earthquakes based on a stochastic finite-fault model, *Bull. Seismol. Soc. Am.*, *92*(5), 1923–1932.

Hayes, G. P., Wald D. J., Johnson R. L. (2012), Slab1. 0: A three-dimensional model of global subduction zone geometries, *J. Geophys. Res.*, *117*, B01302, doi:10.1029/2011JB008524.

Hill, E. M., et al. (2012), The 2010 Mw 7.8 Mentawai earthquake: Very shallow source of a rare tsunami earthquake determined from tsunami field survey and near-field GPS data, *J. Geophys. Res.*, *117,* B06402, doi:10.1029/2012JB009159.

Hoshiba, M., and T. Ozaki (2014), Earthquake early warning and tsunami warning of the Japan Meteorological Agency, and their performance in the 2011 off the Pacific Coast of Tohoku earthquake (Mw 9.0), in *Early Warning for Geological Disasters*, pp. 1–28, Springer, Berlin.

Ichinose, G. A., H. K. Thio, and P. G. Somerville (2004), Rupture process and near-source shaking of the 1965 Seattle-Tacoma and 2001 Nisqually, intraslab earthquakes, *Geophys. Res. Lett.*, *31,* L10604, doi:10.1029/2004GL019668.

Kamai, R., and N. Abrahamson (2015), Are near-fault fling effects captured in the new NGA West2 ground motion models?, *Earthquake Spectra*, *31*(3), 1629–1645.

Kiser, E., and M. Ishii (2012), The March 11, 2011 Tohoku-oki earthquake and cascading failure of the plate interface, *Geophys. Res. Lett.*, *39,* L00G25, doi:10.1029/2012GL051170.

Kurahashi, S., and K. Irikura (2011), Source model for generating strong ground motions during the 2011 off the Pacific coast of Tohoku Earthquake, *Earth Planets Space*, *63*(7), 571–576.

Lay, T., H. Kanamori, C. J. Ammon, K. D. Koper, A. R. Hutko, L. Ye, H. Yue, and T. M. Rushing (2012), Depth-varying rupture properties of subduction zone megathrust faults, *J. Geophys. Res.*, *117*, B04311, doi:10.1029/2011JB009133.

LeVeque, R. J., K. Waagan, F. I. González, D. Rim, and G. Lin (2016), Generating random earthquake events for probabilistic tsunami hazard assessment, *Pure Appl. Geophys.*, doi:10.1007/s00024-016-1357-1.

Li, W. H., M. Lisowski, M. Magee, G. Marshall, M. Murray, R. McPherson, and B. Romanowicz (1993), The Cape Mendocino, California, earthquakes of April 1992: Subduction at the triple junction, *Science*, *261*, 23.

Liu, P., R. J. Archuleta, and S. H. Hartzell (2006), Prediction of broadband ground-motion time histories: Hybrid low/high-frequency method with correlated random source parameters, *Bull. Seismol. Soc. Am.*, *96*(6), 2118–2130.

Mai, P. M., and G. C. Beroza (2000), Source scaling properties from finite-fault-rupture models. *Bull. Seismol. Soc. Am.*, *90*(3), 604–615.

Mai, P. M., and G. C. Beroza (2002), A spatial random field model to characterize complexity in earthquake slip, *J. Geophys. Res.*, *107*(B11), doi:10.1029/2001JB000588.

McCaffrey, R., A. I. Qamar, R. W. King, R. Wells, G. Khazaradze, C. A. Williams, C. W. Stevens, J. J. Vollick, and P. C. Zwick (2007), Fault locking, block rotation and crustal deformation in the Pacific Northwest, *Geophys. J. Int.*, *169*(3), 1315–1340.

McCrory, P. A., J. L. Blair, F. Waldhauser, and D. H. Oppenheimer (2012), Juan de Fuca slab geometry and its relation to Wadati-Benioff zone seismicity, *J. Geophys. Res.*, *117*, B09306, doi:10.1029/2012JB009407.

Melgar, D., and Y. Bock (2015), Kinematic earthquake source inversion and tsunami runup prediction with regional geophysical data, *J. Geophys. Res. Solid Earth*, *120*, 3324–3349, doi:10.1002/2014JB011832.

Melgar, D., Y. Bock, D. Sanchez, and B. W. Crowell (2013), On robust and reliable automated baseline corrections for strong motion seismology, *J. Geophys. Res. Solid Earth*, *118*, 1177–1187, doi:10.1002/jgrb.50135.

Melgar, D., B. W. Crowell, J. Geng, R. M. Allen, Y. Bock, S. Riquelme, E. M. Hill, M. Protti, and A. Ganas (2015), Earthquake magnitude calculation without saturation from the scaling of peak ground displacement, *Geophys. Res. Lett.*, *42*, 5197–5205, doi:10.1002/2015GL064278.

Melgar, D., et al. (2016a), Local tsunami warnings: Perspectives from recent large events, *Geophys. Res. Lett.*, *43*, 1109–1117, doi:10.1002/2015GL067100.

Melgar, D., et al. (2016b), Slip segmentation and slow rupture to the trench during the 2015, Mw8. 3 Illapel, Chile earthquake, *Geophys. Res. Lett.*, *43*, 961–966, doi:10.1002/2015GL067369.

Mena, B., P. M. Mai, K. B. Olsen, M. D. Purvance, and J. N. Brune (2010), Hybrid broadband ground-motion simulation using scattering Green's functions: Application to large-magnitude events, *Bull. Seismol. Soc. Am.*, *100*(5A), 2143–2162.

Minson, S. E., J. R. Murray, J. O. Langbein, and J. S. Gomberg (2014), Real-time inversions for finite fault slip models and rupture geometry based on high-rate GPS data, *J. Geophys. Res. Solid Earth*, *119*, 3201–3231, doi:10.1002/2013JB010622.

Ohta, Y., et al. (2012), Quasi real-time fault model estimation for near-field tsunami forecasting based on RTK-GPS analysis: Application to the 2011 Tohoku-Oki earthquake (Mw 9.0), *J. Geophys. Res.*, *117,* B2311, doi:10.1029/2011JB008750.

Olsen, K. B., W. J. Stephenson, and A. Geisselmeyer (2008), 3D crustal structure and long-period ground motions from a M9. 0 megathrust earthquake in the Pacific Northwest region, *J. Seismol.*, *12*(2), 145–159.

Satake, K., K. Wang, and B. F. Atwater (2003), Fault slip and seismic moment of the 1700 Cascadia earthquake inferred from Japanese tsunami descriptions, *J. Geophys. Res.*, *108*(B11), 2535, doi:10.1029/2003JB002521.

Sieh, K., D. H. Natawidjaja, A. J. Meltzner, C. C. Shen, H. Cheng, K. S. Li, B. W. Suwargadi, J. Galetzka, B. Philibosian, and R. L. Edwards (2008), Earthquake supercycles inferred from sea-level changes recorded in the corals of west Sumatra, *Science*, *322*(5908), 1674–1678.

Simons, M., et al. (2011), The 2011 magnitude 9.0 Tohoku-Oki earthquake: Mosaicking the megathrust from seconds to centuries, *Science*, *332*(6036), 1421–1425.

Somerville, P., K. Irikura, R. Graves, S. Sawada, D. Wald, N. Abrahamson, Y. Iwasaki, T. Kagawa, N. Smith, and A. Kowada (1999), Characterizing crustal earthquake slip models for the prediction of strong ground motion, *Seismol. Res. Lett.*, *70*(1), 59–80.

Tinti, E., E. Fukuyama, A. Piatanesi, and M. Cocco (2005), A kinematic source-time function compatible with earthquake dynamics, *Bull. Seismol. Soc. Am.*, *95*(4), 1211–1223.

Zhu, L. P., and L. A. Rivera (2002), A note on the dynamic and static displacements from a point source in multilayered media, *Geophys. J. Int.*, *148*, 619–627, doi:10.1046/j.1365-246X.2002.01610.x.